






Article

Redox-Modulations of Photophysical and Single-molecule Magnet Properties in Ytterbium Complexes Involving Extended-TTF Triads

Bertrand Lefeuvre ¹, Jessica Flores Gonzalez ¹, Frédéric Gendron ¹, Vincent Dorcet ¹, François Riobé ² , Vladimir Cherkasov ³ , Olivier Maury ², Boris Le Guennic ¹ , Olivier Cador ¹, Viacheslav Kuropatov ^{3,*}  and Fabrice Pointillart ^{1,*} 

¹ Univ Rennes, CNRS, ISCR (Institut des Sciences Chimiques de Rennes)—UMR 6226, 35000 Rennes, France; bertrand.lefeuvre@univ-rennes1.fr (B.L.); jessica.flores-gonzales@univ-rennes1.fr (J.F.G.); frederic.gendron@univ-rennes1.fr (F.G.); vincent.dorcet@univ-rennes1.fr (V.D.); boris.leguennic@univ-rennes1.fr (B.L.G.); olivier.cador@univ-rennes1.fr (O.C.)

² Univ Lyon, Ens de Lyon, CNRS UMR 5182, Université Claude Bernard Lyon 1, Laboratoire de Chimie, F69342 Lyon, France; francois.riobe@ens-lyon.fr (F.R.); olivier.maury@ens-lyon.fr (O.M.)

³ G. A. Razuvaev Institute of Organometallic Chemistry of Russian Academy of Sciences, GSP-445, Tropinina str. 49, 603950 Nizhny Novgorod, Russia; cherkasov@iomc.ras.ru

* Correspondence: viach@iomc.ras.ru (V.K.); fabrice.pointillart@univ-rennes1.fr (F.P.); Tel.: +79-(0)51902995 (V.K.); Tel.: +33-(0)223236752 (F.P.)

Academic Editors: Dawid Pinkowicz and Robert Podgajny

Received: 20 December 2019; Accepted: 22 January 2020; Published: 23 January 2020



Abstract: The reaction between the 2,2'-benzene-1,4-diylbis(6-hydroxy-4,7-di-*tert*-butyl-1,3-benzodithiol-2-yl-ium-5-olate triad (**H₂SQ**) and the metallo-precursor [Yb(hfac)₃]·2H₂O led to the formation of a dinuclear coordination complex of formula [Yb₂(hfac)₆(**H₂SQ**)]·0.5CH₂Cl₂ (**H₂SQ-Yb**). After chemical oxidation of **H₂SQ** in 2,2'-cyclohexa-2,5-diene-1,4-diylidenebis(4,7-di-*tert*-butyl-1,3-benzodithiole-5,6-dione (**Q**), the latter triad reacted with the [Yb(hfac)₃]·2H₂O precursor to give the dinuclear complex of formula [Yb₂(hfac)₆(**Q**)] (**Q-Yb**). Both dinuclear compounds have been characterized by X-ray diffraction, DFT optimized structure and electronic absorption spectra. They behaved as field-induced Single-Molecule Magnets (SMMs) nevertheless the chemical oxidation of the semiquinone to quinone moieties accelerated by a factor of five the relaxation time of the magnetization of **Q-Yb** compared to the one for **H₂SQ-Yb**. The **H₂SQ** triad efficiently sensitized the Yb^{III} luminescence while the chemical oxidation of **H₂SQ** into **Q** induced strong modification of the absorption properties and thus a quenching of the Yb^{III} luminescence for **Q-Yb**. In other words, both magnetic modulation and luminescence quenching are reached by the oxidation of the protonated semiquinone into quinone.

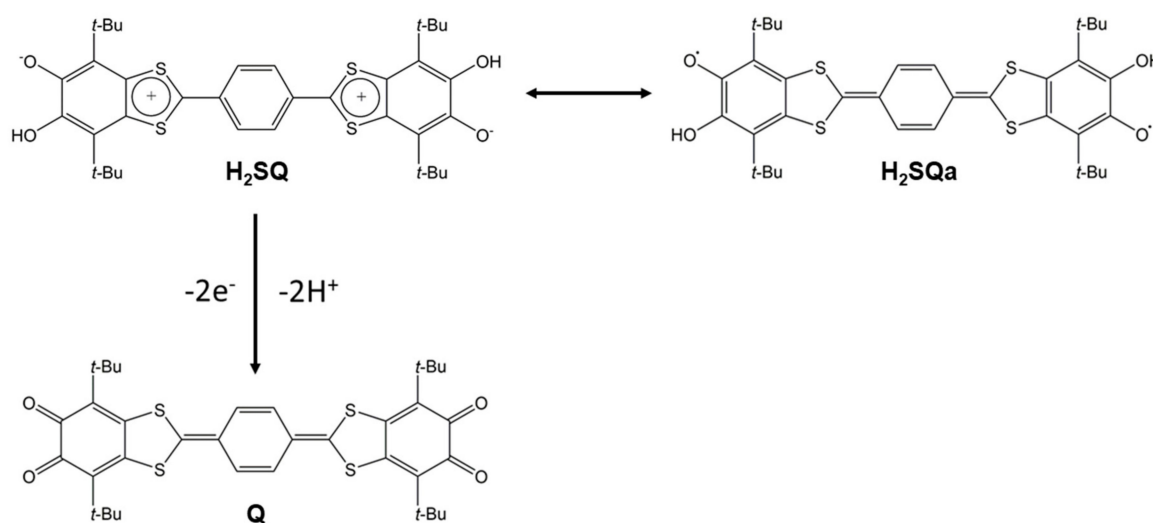
Keywords: ytterbium; extended-tetrathiafulvalene; electro-activity; single-molecule magnet; luminescence

1. Introduction

Molecular magnetism is in intense expansion since the discovery of the first Single-Molecule Magnet (SMM) behavior for a Mn₁₂ cluster [1] and a decade later the similar magnetic behavior for a mononuclear lanthanide complex [2]. The motivation for this kind of nanomagnets comes from the potential applications in high density data storage [3,4] especially since the development of organometallic chemistry allowing the discovery of “high blocking temperature” SMM [5–8]. The magnetic properties of the lanthanide ions strongly depend on the crystal field and slight variations of the electronic distribution of the lanthanides’ surrounding, making such ions excellent candidates for magnetic switches [9–18]. Among the possible magnetic property switches, those playing with oxidation-reduction reactions are the most promising because such a stimulus can lead to drastic

modifications in the electronic properties of the molecular system. Oxidation-reduction reactions can be achieved thanks to redox-active metal centers [19–21] or/and organic ligands [22–24]. Lanthanides are also well-known for their luminescence ranging from the visible to the near infrared (NIR) region [25,26]. The sensitization of their emission is achieved by antenna effect involving singlet [27,28] and triplet [29–31] states of a (metallo)organic chromophore which can be energetically changed by oxido-reduction reaction leading to redox commutation of the NIR luminescence [32–35].

In this article, we proposed to exploit the ligand 2,2'-benzene-1,4-diylbis(6-hydroxy-4,7-di-*tert*-butyl-1,3-benzodithiol-2-yl-5-olate) [36] (**H₂SQ**) (Scheme 1), which is suitable for lanthanide coordination, [37] and its oxidized form 2,2'-cyclohexa-2,5-diene-1,4-diylidenebis(4,7-di-*tert*-butyl-1,3-benzodithiole-5,6-dione) (**Q**) (Scheme 1) to modulate both photophysical and magnetic properties of their corresponding complexes [Yb₂(hfac)₆(**H₂SQ**)]·0.5CH₂Cl₂ (**H₂SQ-Yb**) and [Yb₂(hfac)₆(**Q**)] (**Q-Yb**) (hfac[−] = 1,1,1,5,5,5-hexafluoroacetylacetonate).



Scheme 1. Molecular structures of the **H₂SQ** and **Q** ligands and intramolecular electron transfer in **H₂SQ**.

2. Results and Discussion

2.1. X-Ray Structures

The coordination reaction of the 2,2'-benzene-1,4-diylbis(6-hydroxy-4,7-di-*tert*-butyl-1,3-benzodithiol-2-yl-5-olate) triad (**H₂SQ**) (Scheme 1) and tris(1,1,1,5,5,5-hexafluoro-acetylacetonate)bis (aqueous) Yb^{III} (Yb(hfac)₃·2H₂O) in CH₂Cl₂ led to the formation of the dinuclear complex of formula [Yb₂(hfac)₆(**H₂SQ**)]·0.5CH₂Cl₂ (**H₂SQ-Yb**). The oxidized form of **H₂SQ** was obtained using an excess of MnO₂, the resulting **Q** ligand (Scheme 1) was immediately reacted with Yb(hfac)₃·2H₂O leading to the dinuclear complex [Yb₂(hfac)₆(**Q**)] (**Q-Yb**).

2.1.1. [Yb₂(hfac)₆(**H₂SQ**)]·0.5CH₂Cl₂ (**H₂SQ-Yb**)

H₂SQ-Yb crystallizes in the monoclinic space group P2₁/c (No. 14) (Figure 1 and Figure S1, Table S1). The asymmetric unit is composed by one molecule of [Yb₂(hfac)₆(**H₂SQ**)] and one half dichloromethane molecule of crystallization. The Yb(hfac)₃ units are linked to the two terminal monoprotonated semiquinone coordination sites. A bischelating coordination mode is observed through both C-O[−] and C-OH groups (Figure 1). The coordination strength with the C-O[−] is stronger than the one with C-OH as attested by the Yb-OH distances (2.408(5) Å) which are much longer than the Yb-O[−] distances (2.178(4) Å). The limit case in which the coordination reaction takes place only through the C-O[−] group has been recently observed [37]. The analysis of the C-OH (1.374(7) Å)

and C-O⁻ (1.295(7) Å) bond lengths agrees with the protonated form of the semiquinone moieties. In order to confirm the oxidation state of the triad, the bond lengths of the ligand are carefully analyzed since an intramolecular electron transfer can take place from H₂SQ to H₂SQa (Scheme 1). The 1,3-dithiole rings in H₂SQ-Yb is essentially aromatic since the S1-C15 (1.692(6) Å), S2-C15 (1.660(6) Å), S3-C22 (1.673(7) Å) and S4-C22 (1.671(6) Å) bond lengths are comparable with those for TTF dications (1.670–1.690 Å) while they are longer in neutral TTF (1.730–1.760 Å) [38–40]. The dicationic character of the extended TTF induced a single character of the C15-C16 and C21-C22 bonds as observed with the distances of 1.445(8) Å and 1.458(8) Å. The bond lengths distribution in the terminal six-membered rings in bridging ligand in H₂SQ-Yb is also different from typical o-quinone distribution. The shortest distances in these rings were observed for bonds connecting *t*-Bu-substituted and carbonyl carbon atoms.

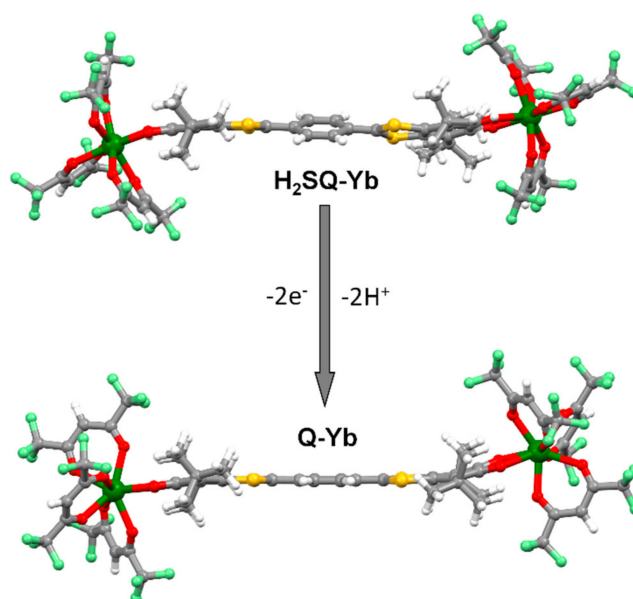


Figure 1. Experimental molecular structure of H₂SQ-Yb and DFT optimized structure of its oxidized form Q-Yb. Molecules of crystallization are omitted for clarity.

Finally, the protonated semiquinone form of the triad with charge-separated structure is also confirmed by the non-planarity of the ligand since the central *p*-phenylene ring and the two 6-hydroxy-4,7-di-*tert*-butyl-1,3-benzodithiol moieties formed a torsion angle of 26.2(2)° in agreement with the one found in the X-ray structure of the free H₂SQ ligand [36]. Thus each Yb^{III} ion is surrounded by eight oxygen atoms coming from the three hfac⁻ anions and the bischelating H₂SQ ligand. The coordination sphere around the metal center can be described as distorted triangular dodecahedron (D_{2d} symmetry) (SHAPE analysis, Table S2) [41].

The crystal packing reveals a good isolation of the two inorganic and organic sub-networks since nor π - π interaction either S \cdots S contact are identified (Figure 2) which is quite unusual for this kind of π -extended sulfured systems. The integrity of the crystal is assumed by H \cdots F interactions. The Yb-Yb intramolecular distance is 21.477 Å while the shortest Yb-Yb intermolecular distance is 10.000 Å.

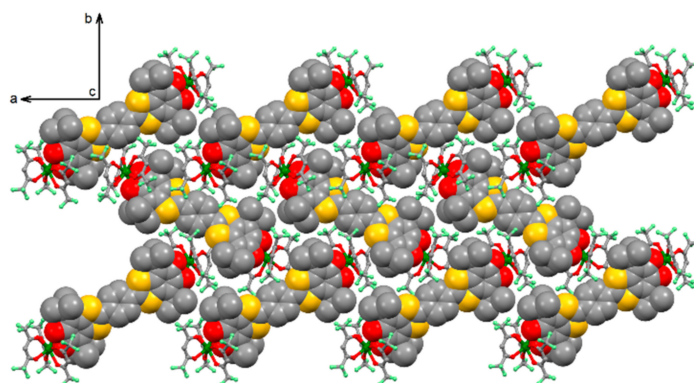


Figure 2. Crystal packing of $\text{H}_2\text{SQ-Yb}$ in the (110) plane. “Spacefill” and “ball and sticks” representations are used for H_2SQ ligands and $\text{Yb}(\text{hfac})_3$ units, respectively.

2.1.2. $[\text{Yb}_2(\text{hfac})_6(\text{Q})]$ (Q-Yb)

Despite all the attempts to obtain suitable single crystals of Q-Yb for diffraction studies, we did not succeed. Consequently based on the X-ray structure of a previous system associated $\text{Yb}(\text{hfac})_3$ unit and quinone-based tetrathiafulvalene ligand [42], the structure of $\text{H}_2\text{SQ-Lu}$ and Q-Lu (Figure 1) have been optimized with the help of DFT (see Experimental Section for computational details and Table S4). The X-ray structure of $\text{H}_2\text{SQ-Yb}$ is well reproduced by the DFT calculations despite the replacement of the $\text{Yb}(\text{III})$ ions by diamagnetic $\text{Lu}(\text{III})$ ions. Only a minor lengthening of the metal-ligand bond lengths is calculated in $\text{H}_2\text{SQ-Lu}$ when compared to $\text{H}_2\text{SQ-Yb}$ (see Table S4). In Q-Lu , the two quinone moieties act as bischelating coordination site. The average six $\text{Lu-O}_{\text{hfac}}$ distances (2.319 Å) are shorter than the average two $\text{Lu-O}_{\text{quinone}}$ ones (2.360 Å) leading to distorted square antiprism (D_{4d}) coordination environment around the Lu^{III} ions (SHAPE analysis, Table S2). The quinone form is confirmed by i) the $\text{C}=\text{O}$ bond length of 1.267 Å shorter than the C-OH and C-O^- observed for the protonated semiquinone form and in agreement with the quinone form previously observed for quinone-based TTF and ii) with the almost planar shape of the Q ligand (torsion angle of 3.7°) because of the increasing of the aromaticity character of the ligand after oxidation. The coordination of the $\text{Yb}(\text{hfac})_3$ units plays a crucial role in the stabilization of the Q ligand since it was previously established that such an oxidized form of the free ligand cannot be isolated in solid-state due to its instability [36]. The Lu-Lu intramolecular distance is 21.664 Å.

2.2. Magnetic Properties

2.2.1. Static Magnetic Measurements

The temperature dependence of $\chi_M T$ for the samples $\text{H}_2\text{SQ-Yb}$ and Q-Yb are given for two Yb^{III} centers and represented in Figure 3. The room temperature values are $4.30 \text{ cm}^3 \cdot \text{K} \cdot \text{mol}^{-1}$ and $5.08 \text{ cm}^3 \text{ K mol}^{-1}$ for $\text{H}_2\text{SQ-Yb}$ and Q-Yb , respectively.

Such values are in the range of observed values for Yb^{III} -based molecular systems [43] and in agreement with the expected value for two Yb^{III} ions ($5.14 \text{ cm}^3 \text{ K mol}^{-1}$, $^2F_{7/2}$ ground state multiplet) [44]. Upon cooling, $\chi_M T$ decreases monotonically down to $2.24 \text{ cm}^3 \cdot \text{K} \cdot \text{mol}^{-1}$ and $2.19 \text{ cm}^3 \text{ K mol}^{-1}$ at 2 K for $\text{H}_2\text{SQ-Yb}$ and Q-Yb , respectively. Taking into account the intra- and intermolecular distance between the metal centers, the decrease of the $\chi_M T$ products is attributed to the thermal depopulation of the M_J states. $\text{H}_2\text{SQ-Yb}$ and Q-Yb exhibited similar magnetization with experimental values of $3.26 \text{ N}\beta$ and $3.34 \text{ N}\beta$ at 50 kOe, respectively [44].

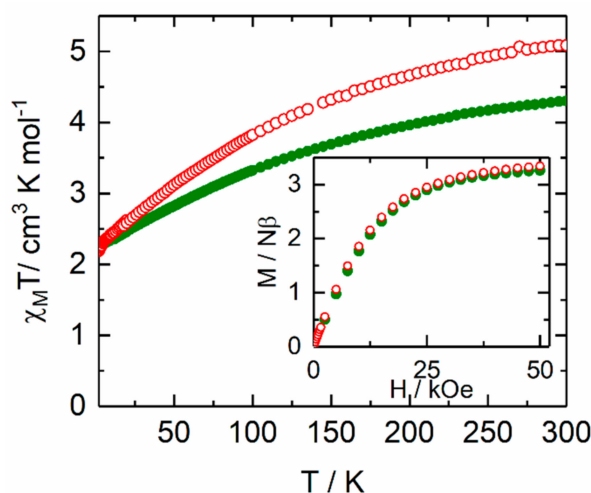


Figure 3. Temperature dependences of $\chi_M T$ for $\text{H}_2\text{SQ-Yb}$ (green) and Q-Yb (red) in applied magnetic field of 10 kOe between 20 and 300 K while a magnetic field of only 2 kOe was used between 2 and 20 K. In inset, the field variations of the magnetization at 2 K for $\text{H}_2\text{SQ-Yb}$ (green) and Q-Yb (red) between 0 and 50 kOe.

2.2.2. Dynamic Magnetic Measurements

The in-phase and out-of-phase components of the ac susceptibility (χ_M'') for both compounds $\text{H}_2\text{SQ-Yb}$ and Q-Yb were measured using immobilized selected and crushed single crystals. For both compounds, any out-of-phase signal was not detected in zero magnetic field in the 1–10000 Hz frequency range. Such absence of out-of-phase component of the ac susceptibility in 0 Oe is common for the Yb^{III} -based coordination complexes because of the fast magnetic relaxation due to efficient Quantum Tunneling of the Magnetization (QTM) which can be cancelled by applying an external magnetic field [45]. Thus the field dependence of the magnetic susceptibility is studied in detail (Figure 4 and Figure S2). For both compounds, the application of a small magnetic field led to the appearance of out-of-phase component of the magnetic susceptibility and the optimal value of the applied magnetic field was chosen thank to the field dependence of the relaxation time (Figure S3). The scan field revealed an unusual behavior since applying a small magnetic field led to the slowest magnetic relaxation of a fraction of the sample (about 50 %) while increasing the value of the applied magnetic field accelerates the magnetic relaxation but increases the relaxing fraction. In fact applying a magnetic field tends to cancel the QTM (appearance of the slow magnetic relaxation fraction) but favor the appearance of field dependent under energy barrier mechanism (direct process). Thus a good compromised magnetic field value could be 800 Oe for $\text{H}_2\text{SQ-Yb}$ while for such field value the maximum was observed at the highest accessible frequency range for Q-Yb at 2 K (Figure 4 and Figure S2).

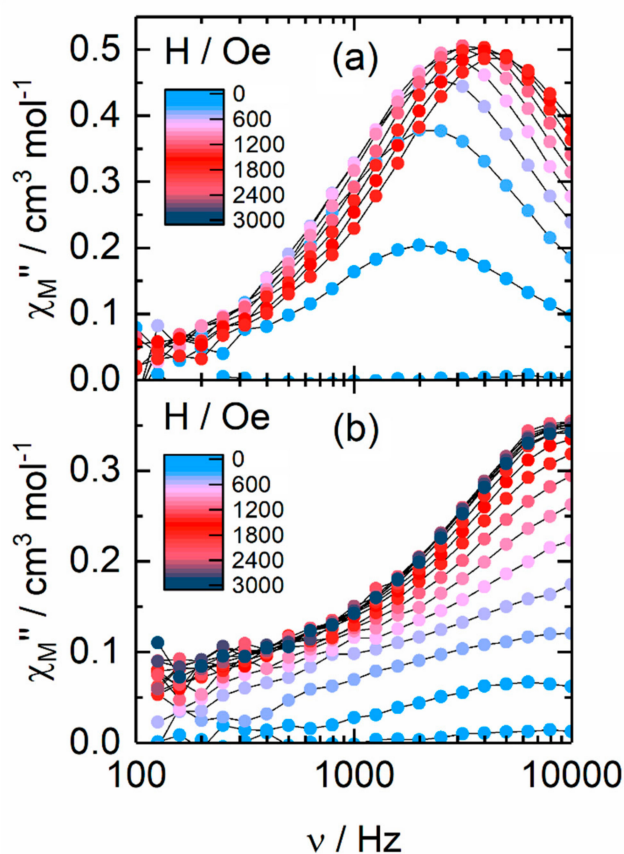


Figure 4. Frequency dependence of χ_M'' between 0 and 3000 Oe for $\text{H}_2\text{SQ-Yb}$ (a) and Q-Yb (b) at 2K.

At this point one can notice that the oxidation of the H_2SQ ligand is accompanied by a fastening of the magnetic relaxation by a factor 5 at 2 K.

Under an applied field of $H = 800$ Oe, $\text{H}_2\text{SQ-Yb}$ highlighted a frequency dependence of the out-of-phase signal of the magnetization (Figure 5a and Figure S4) which can be analyzed in the framework of the extended Debye model [46–48]. The temperature dependence of the relaxation time is extracted (see Supplementary Information for details) and depicted in Figure 5b (Table S3) and the normalized Argand (Figure S5) concluded that at such magnetic field more than 90 % of the sample was slowly relaxing. The relaxation time follows two thermally dependent Orbach and direct processes of relaxation:

$$\tau^{-1} = \tau_0^{-1} \exp(\Delta/T) + BTH^m \quad (1)$$

The best fit was obtained using the Equation (1) with $\tau_0 = 9.25(50) \times 10^{-8}$ s and $\Delta = 10.0(2)$ K, and $B = 1.23(4) \times 10^{-8} \text{ s}^{-1} \text{ K}^{-1} \text{ Oe}^{-4}$ and $m = 4$ (fixed) where Δ is the energy barrier, B and m are constant parameters for the direct relaxation process (Figure 5b). The involvement of direct process is strongly supported by the field dependence of the relaxation time (Figures S2 and S3) and the selected 800 Oe applied magnetic field. All the other attempts to include other magnetic relaxation processes led to a predominant Raman mechanism which exclude both remaining QTM and Direct process (Figures S6–S8). Nevertheless, the field dependence of the magnetic susceptibility (Figures S2–S3) imposed the presence of the Direct process.

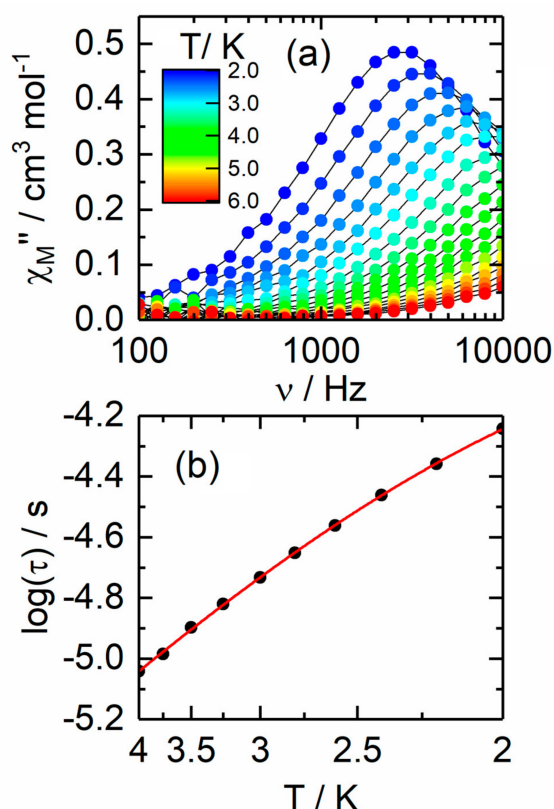


Figure 5. (a) Frequency dependence of χ_M'' between 2 and 6 K for $\text{H}_2\text{SQ-Yb}$ at 800 Oe, (b) Temperature variation of the relaxation time for $\text{H}_2\text{SQ-Yb}$ in the temperature range of 2–4 K with the best fitted curve with the Arrhenius law (red line).

2.2.3. Photophysical Properties

The UV-visible absorption properties for $\text{H}_2\text{SQ-Yb}$ and Q-Yb have been studied in a CH_2Cl_2 solution (Figure 6a). The spectra are dominated by the $\pi\text{-}\pi^*$ $h\nu\text{ac}^-$ transition at high energy (33000 cm^{-1}) and Intra-Ligand Charge Transfers (ILCTs) at low energy. $\text{S} \rightarrow \text{L}$ and $\text{H} \rightarrow \text{L}$ (where S = Single Occupied Molecular Orbital, L = Lowest Unoccupied Molecular Orbital and H = Highest Occupied Molecular Orbital) ILCT have been previously identified for the corresponding free H_2SQ and Q triads with the S and H mainly localized on the extended TTF while L is situated on the semiquinone and quinone acceptors [36,49,50]. Thus for $\text{H}_2\text{SQ-Yb}$ and based on DFT calculations for the free H_2SQ triad [36], the strong absorption band centered at 12500 cm^{-1} is attributed to the $\text{H} \rightarrow \text{L}$ ILCT and the shoulder centered at 20.000 cm^{-1} is attributed to $\text{S} \rightarrow \text{L}$ ILCT. For Q-Yb , the most intense absorption band at 9800 cm^{-1} is attributed to the $\text{H} \rightarrow \text{L}$ ILCT. The oxidation of the $\text{H}_2\text{SQ-Yb}$ into Q-Yb induced a redshift of the $\text{H} \rightarrow \text{L}$ ILCT from 12500 cm^{-1} to 9800 cm^{-1} (average energy value of the maxima). It was previously demonstrated that the low-energy ILCT could be an efficient donating source for sensitization of NIR lanthanide emitters [27,51,52]. Irradiation at 16670 cm^{-1} (or lower energy) induced the expected $^2\text{F}_{5/2} \rightarrow ^2\text{F}_{7/2}$ Yb^{III} emission (Figure 6b) for $\text{H}_2\text{SQ-Yb}$ whereas after the two-electron oxidation the same irradiation highlighted the total quenching of the NIR emission for Q-Yb . The NIR luminescence of $\text{H}_2\text{SQ-Yb}$ is composed of four components as expected from the splitting of the $^2\text{F}_{7/2}$ ground state by the ligand field effect [53–55] localized at 10157 cm^{-1} , 9926 cm^{-1} , 9639 cm^{-1} and 9560 cm^{-1} (Figure 6b). Since the emission of the lanthanide ions can be interpreted as a photography of the ground state energy splitting, the experimental energy barrier determined from the energy gap between the ground and the first excited states is 231 cm^{-1} (332 K) which is much more higher than the value determined from the magnetic properties (10 K). Such observation may signify that the Orbach contribution is negligible and the magnetic relaxation occurs mainly through the direct process.

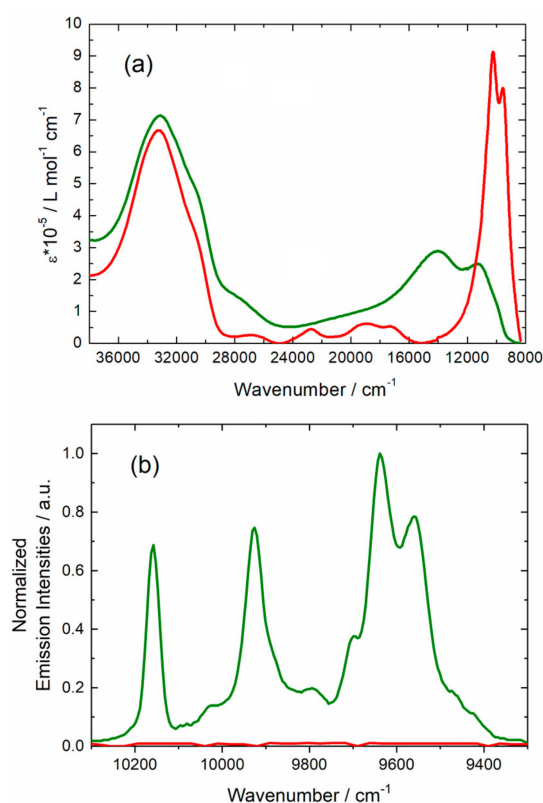
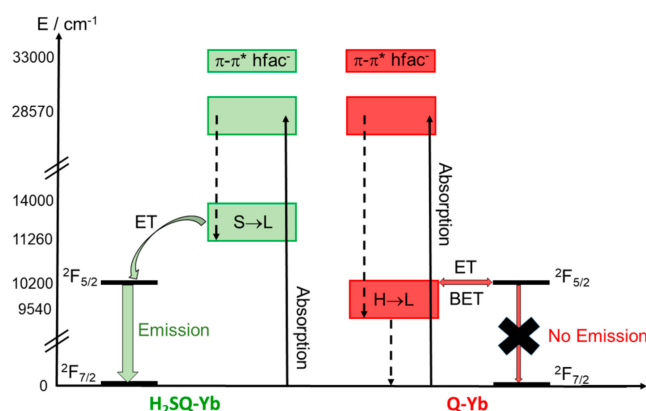


Figure 6. (a) Experimental UV-visible absorption spectra at room temperature of $\text{H}_2\text{SQ-Yb}$ (green line) and Q-Yb (red line) in CH_2Cl_2 solution ($C = 4 \times 10^{-5} \text{ mol.L}^{-1}$). (b) Emission spectra at 77 K of $\text{H}_2\text{SQ-Yb}$ (green line) and Q-Yb (red line) for an irradiation energy of 16670 cm^{-1} in solid-state.

The efficiency of the NIR emission sensitization strongly depends on the energy position of the ILCT. The donating ILCT ($\text{S} \rightarrow \text{L}$ in Scheme 2) in $\text{H}_2\text{SQ-Yb}$ is localized 2300 cm^{-1} above the emitting ${}^2\text{F}_{5/2}$ level which is well suited for an efficient sensitization while both donating and emitting levels are localized at the same energy in Q-Yb leading to efficient back energy transfer (BET) and thus a quenching of the NIR emission.



Scheme 2. Proposed sensitization process in $\text{H}_2\text{SQ-Yb}$ (left part) and Q-Yb (right part). Dashed lines represent the non-radiative deactivations, ET = Energy Transfer, BET = Back Energy Transfer, H = HOMO, L = LUMO and S = SOMO.

3. Materials and Methods

3.1. Synthesis. General Procedures and Materials

The precursor $\text{Dy}(\text{hfac})_3 \cdot 2\text{H}_2\text{O}$ ($\text{hfac}^- = 1,1,1,5,5,5$ -hexafluoroacetate anion) and the 2,2'-benzene-1,4-diylbis(6-hydroxy-4,7-di-*tert*-butyl-1,3-benzodithiol-2-ylidene-5-olate ligand (**H₂SQ**) were synthesized following previously reported methods [36,56]. All other reagents were commercially available and used without further purification.

3.2. Synthesis of complexes $[\text{Yb}_2(\text{hfac})_6(\text{H}_2\text{SQ})] \cdot 0.5\text{CH}_2\text{Cl}_2$ (**H₂SQ-Yb**) and $[\text{Yb}_2(\text{hfac})_6(\text{Q})]$ (**Q-Yb**)

$[\text{Yb}_2(\text{hfac})_6(\text{H}_2\text{SQ})] \cdot 0.5\text{CH}_2\text{Cl}_2$ (**H₂SQ-Yb**). 66.4 mg of $\text{Yb}(\text{hfac})_3 \cdot 2\text{H}_2\text{O}$ (0.08 mmol) were dissolved in 10 mL of CH_2Cl_2 and then added to a purple solution of 10 mL of CH_2Cl_2 containing 26.4 mg of **H₂SQ** (0.04 mmol). The purple solution of **H₂SQ** immediately turned blue with the addition of the Yb^{III} salt. After 15 minutes of stirring, 20 mL of *n*-hexane were layered at room temperature in the dark. Slow diffusion leads to dark blue single crystals of **H₂SQ-Yb** which are suitable for X-ray studies. Yield (determined from isolated single crystals) 40.4 mg (44 %). Anal. Calcd (%) for $\text{C}_{66.5}\text{H}_{49}\text{Yb}_2\text{F}_{36}\text{O}_{16}\text{S}_4\text{Cl}$: C 37.73, H 2.13; found: C 38.09, H 2.22.

$[\text{Yb}_2(\text{hfac})_6(\text{Q})]$ (**Q-Yb**). 13.2 mg of **H₂SQ** (0.02 mmol) were dissolved in 20 mL of CH_2Cl_2 and then stirred in presence of 1.5 g of MnO_2 . The starting purple solution turned green (oxidation of **H₂SQ** into **Q**) and after 45 min of stirring it was filtered directly in a CH_2Cl_2 solution (5 mL) of $\text{Yb}(\text{hfac})_3 \cdot 2\text{H}_2\text{O}$ (33.2 mg, 0.04 mmol). The green solution turned to a dark pink color. Addition of *n*-pentane into the resulting dark pink solution led to formation of a dark pink crystalline powder. Yield 32.0 mg (71 %). Anal. Calcd (%) for $\text{C}_{66}\text{H}_{46}\text{Yb}_2\text{F}_{36}\text{O}_{16}\text{S}_4$: C 35.18, H 2.04; found: C 35.66, H 2.19.

3.3. Crystallography

Single crystal of **H₂SQ-Yb** was mounted on a APEXIII D8 VENTURE AXS diffractometer for data collection (Bruker, Billerica, MA, USA), MoK_α radiation source, $\lambda = 0.71073 \text{ \AA}$, from the Centre de Diffractométrie (CDIFX), Université de Rennes 1, France (Table S1). Structure was solved with a direct method using the SHELXT program [57] and refined with a full matrix least-squares method on F^2 using the SHELXL-14/7 program [58]. Complete crystal structure results as a CIF file including bond lengths, angles, and atomic coordinates are deposited as Supporting Information. CCDC number is 1970010 for compound **H₂SQ-Yb**.

3.4. Physical Measurements

The elemental analyses of the compounds were performed at the Centre Régional de Mesures Physiques de l'Ouest, Rennes, France. Absorption spectra were recorded on a V-650 spectrophotometer (JASCO, Easton, MD, USA) in dilute solutions, using spectrophotometric grade solvents. Emission spectra were measured using Fluorolog-3 fluorimeter (Horiba-Jobin-Yvon, Kyoto, Japan). The steady-state luminescence was excited by unpolarized light from a 450 W xenon continuous wave (CW) lamp and detected at an angle of 90° by a nitrogen-cooled InGAs detector (Horiba-Jobin-Yvon, Kyoto, Japan). Quartz tubes containing solid samples of each compound were placed in a quartz dewar containing liquid nitrogen. The dc magnetic susceptibility measurements were performed on solid polycrystalline samples with a MPMS-XL SQUID magnetometer (Quantum Design Inc., San Diego, CA, USA) between 20 and 300 K in applied magnetic field of 2 kOe between 2 and 20 K and 10 kOe above. The microcrystallites are immobilized in a pellet made with Teflon tape. These measurements were all corrected for the diamagnetic contribution as calculated with Pascal's constants. The ac magnetic susceptibility measurements were performed on a Quantum Design PPMS (Quantum Design Inc., San Diego, CA, USA) system equipped with ac/dc probe.

3.5. Computational Details

The structure optimization of **Q-Yb** was carried out at the Kohn-Sham density functional theory (DFT) level with the Amsterdam Density Functional (ADF) [59–61] software package. In this calculation,

the Yb³⁺ center was replaced by the closed-shell Lu³⁺ ion, and the scalar all-electron zeroth-order regular approximation (ZORA) [62] was employed for the treatment of the scalar relativistic effects. The PBE functional (Perdew-Burke-Ernzerhof) [63] from the generalized gradient approximation, was used along with the triple- ζ polarized Slater type orbital (STO) all-electron basis set with one set of polarization function for all atoms (TZP) [64].

4. Conclusions

In this article, the 2,2'-benzene-1,4-diylbis(6-hydroxy-4,7-di-*tert*-butyl-1,3-benzodithiol-2-ylidene-5-olate triad (**H₂SQ**) allowed the formation of a dinuclear complex of formula [Yb₂(hfac)₆(**H₂SQ**)]·0.5CH₂Cl₂ (**H₂SQ-Yb**) in which the two Yb^{III} ions are coordinated to the bischelating protonated semiquinone units. After the chemical oxidation of the **H₂SQ** triad, the resulting 2,2'-cyclohexa-2,5-diene-1,4-diylidenebis(4,7-di-*tert*-butyl-1,3-benzodithiole-5,6-dione **Q** triad allowed the formation of a new dinuclear complex [Yb₂(hfac)₆(**Q**)] (**Q-Yb**). The two-electron oxidation of the triad induced changes in the electronic absorption spectra with a red shift of the ILCT bands. For **H₂SQ-Yb**, irradiation of the ILCT induced an efficient sensitization of the Yb^{III} NIR emission while the lower-energy ILCT for **Q-Yb** allowed back energy transfer and so a quenching of the NIR emission. Both compounds behave as field-induced SMM with a fastening of the magnetic relaxation after oxidation. In conclusion the oxidation of the **H₂SQ** triad into the **Q** one induced a dual magnetic modulation and luminescence quenching.

Supplementary Materials: The following are available online at <http://www.mdpi.com/1420-3049/25/3/492/s1>, Figure S1. ORTEP view of the asymmetric unit in [Yb₂(hfac)₆(**H₂SQ**)]·0.5CH₂Cl₂ (**H₂SQ-Yb**). Thermal ellipsoids are drawn at 30% probability. Hydrogen atoms and CH₂Cl₂ molecule of crystallization are omitted for clarity. Figure S2. Scan field of the frequency dependence of the in phase (χ_M') component of the ac magnetic susceptibility for **H₂SQ-Yb** (a) and **Q-Yb** (b). Figure S3. Field dependence of the magnetic relaxation time of **H₂SQ-Yb**. Figure S4. Frequency dependence of the in-phase component of the magnetic susceptibility for **H₂SQ-Yb** measured under a DC applied magnetic field of 800 Oe in the 2–6 K temperature range. Figure S5. Normalized Cole-Cole plots for **H₂SQ-Yb** at several temperatures between 2 and 3 K. Table S1: X-ray crystallographic data for **H₂SQ-Yb**. Table S2: SHAPE analysis of the coordination polyhedra around the lanthanide in **H₂SQ-Yb** and **Q-Yb**.; Table S3: Best fitted parameters (χ_T , χ_S , τ and α) with the extended Debye model for compound **H₂SQ-Yb** at 800 Oe in the temperature range 2–4 K.

Author Contributions: V.C. and V.K. performed the organic syntheses; B.L. performed the coordination chemistry and crystallizations; V.D. realized the single crystal X-ray diffraction experiments and structure refinements; O.C. and J.F.G. performed and analyzed the magnetic measurements, F.R. and O.M. performed the photophysical measurements, F.G. and B.L.G. performed the DFT calculations, F.P. conceived and designed the experiments; F.P., O.C., V.K. and B.L.G. contributed to the writing of the article. All authors have read and agreed to the published version of the manuscript.

Funding: This work was supported by Région Bretagne, Rennes Métropole, CNRS, Université de Rennes 1, France-Russia MULTISWITCH PRC Grant (No. 199001), RFBR according to the research project No. 18-53-15004, the Russian state assignment, and the European Commission through the ERC-CoG 725184 MULTIPROSMM (project No. 725184). B.L.G. and F.G. thank the French GENCI/IDRIS-CINES center for high-performance computing resources.

Conflicts of Interest: The authors declare no conflict of interest. The founding sponsors had no role in the design of the study; in the collection, analyses, or interpretation of data; in the writing of the manuscript, and in the decision to publish the results.

References

1. Sessoli, R.; Gatteschi, D.; Caneschi, A.; Novak, M.A. Magnetic bistability in a metal-ion cluster. *Nature* **1993**, *365*, 141–143. [[CrossRef](#)]
2. Ishikawa, N.; Sugita, M.; Ishikawa, T.; Koshihara, S.-Y.; Kaizu, Y. Lanthanide Double-Decker Complexes Functioning as Magnets at the Single-Molecular Level. *J. Am. Chem. Soc.* **2003**, *125*, 8694–8695. [[CrossRef](#)]
3. Mannini, M.; Pineider, F.; Sainctavit, P.; Danieli, C.; Otero, E.; Sciancalepore, C.; Talarico, A.M.; Arrio, M.-A.; Cornia, A.; Gatteschi, D.; et al. Magnetic memory of a single-molecule quantum magnet wired to a gold surface. *Nat. Mater.* **2009**, *8*, 194–197. [[CrossRef](#)]
4. Affronte, M. Molecular nanomagnets for information technologies. *J. Mater. Chem.* **2009**, *19*, 1731–1737. [[CrossRef](#)]

5. Guo, F.-S.; Day, B.-M.; Chen, Y.-C.; Tong, M.-L.; Mansikkamäki, A.; Layfield, R.A. A Dysprosium Metallocene Single-Molecule Magnet Functioning at the Axial Limit. *Angew. Chem. Int. Ed.* **2017**, *56*, 11445–11449. [[CrossRef](#)] [[PubMed](#)]
6. Goodwin, C.A.P.; Ortu, F.; Reta, D.; Chilton, N.F.; Mills, D.P. Molecular magnetic hysteresis at 60 kelvin in dysprosocenium. *Nature* **2017**, *548*, 439–442. [[CrossRef](#)] [[PubMed](#)]
7. McClain, K.R.; Gould, C.A.; Chakarawet, K.; Teat, S.J.; Groshens, T.J.; Long, J.R.; Harvey, B.G. High-temperature magnetic blocking and magneto-structural correlations in a series of dysprosium(III) metallocenium single-molecule magnets. *Chem. Sci.* **2018**, *9*, 8492–8503. [[CrossRef](#)] [[PubMed](#)]
8. Guo, F.-S.; Day, B.-M.; Chen, Y.-C.; Tong, M.-L.; Mansikkamäki, A.; Layfield, R.A. Magnetic hysteresis up to 80 kelvin in a dysprosium metallocene single-molecule magnet. *Science* **2018**, *362*, 1400–1403. [[CrossRef](#)] [[PubMed](#)]
9. Suzuki, K.; Sato, R.; Mizuno, N. Reversible switching of single-molecule magnet behaviors by transformation of dinuclear dysprosium cores in polyoxometalates. *Chem. Sci.* **2013**, *4*, 596–600. [[CrossRef](#)]
10. Liu, J.-L.; Chen, Y.-C.; Zheng, Y.-Z.; Lin, W.-Q.; Ungur, L.; Wernsdorfer, W.; Chibotaru, L.F.; Tong, M.-L. Switching the anisotropy barrier of a single-ion magnet by symmetry change from quasi- D_{5h} to quasi- O_h . *Chem. Sci.* **2013**, *4*, 3310–3316.
11. Zhang, X.; Vieru, V.; Feng, X.; Liu, J.-L.; Zhang, Z.; Na, B.; Shi, W.; Wang, B.-W.; Powell, A.K.; Chibotaru, L.F.; et al. Influence of Guest Exchange on the Magnetization Dynamics of Dilanthanide Single-Molecule-Magnet Nodes within a Metal-Organic Framework. *Angew. Chem. Int. Ed.* **2015**, *54*, 9861–9865. [[CrossRef](#)] [[PubMed](#)]
12. Ge, J.-Y.; Cui, L.; Li, J.; Yu, F.; Song, Y.; Zhang, Y.-Q.; Zuo, J.-L.; Kurmoo, M. Modulation Single-Molecule Magnetic Behavior of a Dinuclear Erbium(III) Complex by Solvent Exchange. *Inorg. Chem.* **2017**, *56*, 336–343. [[CrossRef](#)] [[PubMed](#)]
13. Pinkowicz, D.; Ren, M.; Zheng, L.-M.; Sato, S.; Hasegawa, M.; Morimoto, M.; Irie, M.; Breedlove, B.K.; Cosquer, G.; Katoh, K.; et al. Control of the Single-Molecule Magnet Behavior of Lanthanide-Diarylethene Photochromic Assemblies by Irradiation with Light. *Chem. Eur. J.* **2014**, *20*, 12502–12513. [[CrossRef](#)] [[PubMed](#)]
14. Cosquer, G.; Morimoto, M.; Irie, M.; Fetoh, A.; Breedlove, B.K.; Yamashita, M. Photo-control of the magnetic properties of Dy(III) and Ho(III) homometal coordination polymers bridged by a diarylethene ligand. *Dalton Trans.* **2015**, *44*, 5996–6002. [[CrossRef](#)]
15. Wang, L.-F.; Qiu, J.-Z.; Liu, J.-L.; Chen, Y.-C.; Jia, J.-H.; Jover, J.; Ruiz, E.; Tong, M.-L. Modulation of single-molecule magnet behaviour via photochemical [2+2] cycloaddition. *Chem. Commun.* **2015**, *51*, 15358–15361. [[CrossRef](#)]
16. Selvanathan, P.; Huang, G.; Guizouarn, T.; Roisnel, T.; Fernandez-Garcia, G.; Totti, F.; Le Guennic, B.; Calvez, G.; Bernot, K.; Norel, L.; et al. Highly Axial Magnetic Anisotropy in a N3O5 Dysprosium(III) Coordination Environment Generated by a Merocyanine Ligand. *Chem. Eur. J.* **2016**, *22*, 15222–15226. [[CrossRef](#)]
17. Tian, H.; Su, J.-B.; Bao, S.S.; Kurmoo, M.; Huang, X.-D.; Zhang, Y.-Q.; Zheng, L.-M. Reversible ON-OFF switching of single-molecule-magnetism associated with single-crystal-to-single-crystal structural transformation of a decanuclear dysprosium phosphate. *Chem. Sci.* **2018**, *9*, 6424–6433. [[CrossRef](#)]
18. Liang, Z.; Damjanovic, M.; Kamila, M.; Cosquer, G.; Breedlove, B.K.; Enders, M.; Yamashita, M. Proton Control of the Lanthanoid Single-Ion Magnet Behavior of a Double-Desker Complex with an Indolenine-Substituted Annulene Ligand. *Inorg. Chem.* **2017**, *56*, 6512–6521. [[CrossRef](#)]
19. Zhang, P.; Perfetti, M.; Kern, M.; Hallmen, P.P.; Ungur, L.; Lenz, S.; Ringenberg, M.R.; Frey, W.; Stoll, H.; Rauhut, G.; et al. Exchange coupling and single molecule magnetism in redox-active tetraoxolene-bridged dilanthanide complexes. *Chem. Sci.* **2018**, *9*, 1221–1230. [[CrossRef](#)]
20. Dolinar, B.S.; Gomez-Coca, S.; Alexandropoulos, D.I.; Dunbar, K.R. An air stable radical-bridged dysprosium single molecule magnet and its neutral counterpart: Redox switching of magnetic relaxation dynamics. *Chem. Commun.* **2017**, *53*, 2283–2286. [[CrossRef](#)]
21. Takamatsu, S.; Isikawa, T.; Koshihara, S.Y.; Ishikawa, N. Significant Increase of the Barrier Energy for Magnetization Reversal of a Single-4f-Ionic Single-Molecule Magnet by a Longitudinal Contraction of the Coordination Space. *Inorg. Chem.* **2007**, *46*, 7250–7252. [[CrossRef](#)] [[PubMed](#)]
22. Norel, L.; Feng, M.; Bernot, K.; Roisnel, T.; Guizouarn, T.; Costuas, K.; Rigaut, S. Redox Modulation of Magnetic Slow Relaxation in a 4f-Based Single-Molecule Magnet with a 4d Carbon-Rich Ligand. *Inorg. Chem.* **2014**, *53*, 2361–2363. [[CrossRef](#)] [[PubMed](#)]

23. Dickie, C.M.; Laughlin, A.L.; Wofford, J.D.; Bhuvanesh, N.S.; Nippe, M. Transition metal redox switches for reversible “on/off” and “slow/fast” single-molecule magnet behaviour in dysprosium and erbium bis-diamidoferrocene complexes. *Chem. Sci.* **2017**, *8*, 8039–8049. [[CrossRef](#)] [[PubMed](#)]
24. Cador, O.; Le Guennic, B.; Pointillart, F. Electro-Activity and Magnetic Switching in Lanthanide-Based Single-Molecule Magnets. *Inorg. Chem. Front.* **2019**, *6*, 3398–3417. [[CrossRef](#)]
25. Sy, M.; Nonat, A.; Hildebrandt, N.; Charbonnière, L.J. Lanthanide-based luminescence biolabelling. *Chem. Commun.* **2016**, *52*, 5080–5095. [[CrossRef](#)]
26. Zhang, K.Y.; Yu, Q.; Wei, H.; Liu, S.; Zhao, Q.; Huang, W. Long-Lived Emission Probes for time-Resolved Photoluminescence Bioimaging and Biosensing. *Chem. Rev.* **2018**, *118*, 1770–1839. [[CrossRef](#)]
27. D’Aléo, A.; Pointillart, F.; Ouahab, L.; Andraud, C.; Maury, O. Charge transfer excited states sensitization of lanthanide emitting from the visible to the near-infra-red. *Coord. Chem. Rev.* **2012**, *256*, 1604–1620. [[CrossRef](#)]
28. Pointillart, F.; Le Guennic, B.; Cador, O.; Maury, O.; Ouahab, L. Lanthanide Ion and Tetrathiafulvalene-Based Ligand as a “Magic” Couple toward Luminescence, Single Molecule Magnets, and Magnetostructural Correlations. *Acc. Chem. Res.* **2015**, *48*, 2834–2842. [[CrossRef](#)]
29. Bünzli, J.-C.G.; Piguet, C. Taking advantage of luminescent lanthanide ions. *Coord. Chem. Rev.* **2005**, *34*, 1048–1077. [[CrossRef](#)]
30. Eliseeva, S.V.; Bünzli, J.-C.G. Lanthanide luminescence for functional materials and bio-sciences. *Chem. Soc. Rev.* **2010**, *39*, 189–227. [[CrossRef](#)]
31. Bünzli, J.-C.G. On the design of highly luminescent lanthanide complexes. *Coord. Chem. Rev.* **2015**, *293–294*, 19–47. [[CrossRef](#)]
32. Di Piazza, E.; Norel, L.; Costuas, K.; Bourdolle, A.; Maury, O.; Rigaut, S. D-f Heterobimetallic Association between Ytterbium and Ruthenium Carbon-Rich Complexes: Redox Commutation of Near-IR Luminescence. *J. Am. Chem. Soc.* **2011**, *133*, 6174–6176. [[CrossRef](#)] [[PubMed](#)]
33. Al Sabea, H.; Norel, L.; Galangau, O.; Hijazi, H.; Métivier, R.; Roisnel, T.; Maury, O.; Bucher, C.; Riobé, F.; Rigaut, S. Dual Light and Redox Control of NIR Luminescence with Complementary Photochromic and Organometallic Antennae. *J. Am. Chem. Soc.* **2019**. [[CrossRef](#)] [[PubMed](#)]
34. Tropiano, M.; Kilah, N.L.; Morten, M.; Rahman, H.; Davis, J.J.; Beer, P.D.; Faulkner, S. Reversible Luminescence Switching of a Redox-Active Ferrocene-Europium Dyad. *J. Am. Chem. Soc.* **2011**, *133*, 11847–11849. [[CrossRef](#)] [[PubMed](#)]
35. Molloy, J.K.; Jarjayes, O.; Philouze, C.; Fedele, L.; Imbert, D.; Thomas, F. A redox active switch for lanthanide luminescence in phenolate complexes. *Chem. Commun.* **2017**, *53*, 605–608. [[CrossRef](#)]
36. Chalkov, N.O.; Cherkasov, V.K.; Abakumov, G.A.; Romanenko, G.V.; Ketkov, S.Y.; Smolyaninov, I.V.; Starikov, A.G.; Kuropatov, V.A. Compactly Fused o-Quinone-Extended Tetrathiafulvalene-o-Quinone Triad—A Redox-Amphoteric Ligand. *Eur. J. Org. Chem.* **2014**, 4571–4576. [[CrossRef](#)]
37. Flores Gonzalez, J.; Cador, O.; Ouahab, L.; Norkov, S.; Kuropatov, V.; Pointillart, F. Field-Induced Dysprosium Single-Molecule Magnet Involving a Fused o-Semiquinone-Extended-Tetrathiafulvalene-o-Semiquinone Bridging Triad. *Inorganics* **2018**, *6*, 45. [[CrossRef](#)]
38. Jones, A.E.; Christensen, C.A.; Perepichka, D.F.; Batsanov, A.S.; Beeby, A.; Low, P.J.; Bryce, M.R.; Parker, A.W. Photochemistry of the π -Extended 9,10-Bis(1,3-dithiol-2-ylidene)-9,10-dihydroanthracene System: Generation and Characterisation of the Radical Cation, Dication, and Derived Products. *Chem. Eur. J.* **2001**, *7*, 973–978. [[CrossRef](#)]
39. Cooper, W.F.; Edmonds, J.W.; Wudl, F.; Coppens, P. The 2-2'-bi-1,3-dithiole. *Cryst. Struct. Commun.* **1974**, *3*, 23–26.
40. Ellern, A.; Bernstein, J.; Becker, J.Y.; Zamir, S.; Shahal, L.; Cohen, S. New Polymorphic Modification of tetrathiafulvalene. Crystal Structure, Lattice Energy and Intermolecular Interactions. *Chem. Mater.* **1994**, *6*, 1378–1385. [[CrossRef](#)]
41. Llunell, M.; Casanova, D.; Cirera, J.; Bofill, J.M.; Alemany, P.; Alvarez, S. *SHAPE, Version 2.1.*; Universitat de Barcelona: Barcelona, Spain, 2013.
42. Pointillart, F.; Kuropatov, V.; Mitin, A.; Maury, O.; Le Gal, Y.; Golhen, S.; Cador, O.; Cherkasov, V.; Ouahab, L. Lanthanide-Based Dinuclear Complexes Involving an o-Quinone-Tetrathiafulvalene-o-Quinone Bridging Ligand: X-ray Structures, Magnetic and Photophysical Properties. *Eur. J. Inorg. Chem.* **2012**, 4708–4718. [[CrossRef](#)]
43. Pointillart, F.; Cador, O.; Le Guennic, B.; Ouahab, L. Uncommon lanthanide ions in purely 4f Single Molecule Magnets. *Coord. Chem. Rev.* **2017**, *346*, 150–175. [[CrossRef](#)]

44. Kahn, O. *Molecular Magnetism*; VCH: Weinheim, Germany, 1993.
45. Poneti, G.; Bernot, K.; Bogani, L.; Caneschi, A.; Sessoli, R.; Wernsdorfer, W.; Gatteschi, D. A rational approach to the modulation of the dynamics of the magnetisation in a dysprosium-nitronyl-nitroxide radical complex. *Chem. Commun.* **2007**, 1807–1809. [[CrossRef](#)] [[PubMed](#)]
46. Cole, K.S.; Cole, R.H. Dispersion and absorption in dielectrics I. Alternating current characteristics. *J. Chem. Phys.* **1941**, *9*, 341–351. [[CrossRef](#)]
47. Orbach, R. Spin-lattice relaxation in rare-earth salts. *Proc. R. Soc. Lond. A Math. Phys. Eng. Sci.* **1961**, *264*, 458–484.
48. Orbach, R. On the theory of spin-lattice relaxation in paramagnetic salts. *Proc. Phys. Soc.* **1961**, *77*, 821–826. [[CrossRef](#)]
49. Chalkov, N.O.; Cherkasov, V.K.; Abakumov, G.A.; Starikov, A.G.; Kuropatov, V.A. Protonated paramagnetic redox forms of di-*o*-quinone bridged with *p*-phenylene-extended TTF: A EPR spectroscopy study. *Beilstein J. Org. Chem.* **2016**, *12*, 2450–2456. [[CrossRef](#)]
50. Chalkov, N.O.; Cherkasov, V.K.; Abakumov, G.A.; Starikov, A.G.; Kuropatov, V.A. EPR spectroscopy study of di-*o*-quinone bridged by π -extended TTF: Redox behavior and binding modes as a ligand. *New J. Chem.* **2016**, *40*, 1244–1249. [[CrossRef](#)]
51. Ziessel, R.; Ulrich, G.; Charbonnière, L.; Imbert, D.; Scopelliti, R.; Bünzli, J.-C.G. NIR Lanthanide Luminescence by Energy Transfer from Appended Terpyridine-Boradiazaindacene Dyes. *Chem. Eur. J.* **2006**, *12*, 5060–5067. [[CrossRef](#)]
52. Pointillart, F.; Cauchy, T.; Maury, O.; Le Gal, Y.; Golhen, S.; Cador, O.; Ouahab, L. Tetrathiafulvalene-amido-2-pyridine-N-oxide as Efficient Charge-Transfer Antenna Ligand for the Sensitization of Yb^{III} Luminescence in a Series of Lanthanide Paramagnetic Coordination Complexes. *Eur. J. Chem.* **2010**, *16*, 11926–11941. [[CrossRef](#)]
53. Bünzli, J.-C.G. Benefiting from the Unique Properties of Lanthanide Ions. *Acc. Chem. Res.* **2006**, *39*, 53–61. [[CrossRef](#)] [[PubMed](#)]
54. Eliseeva, S.V.; Bünzli, J.-C.G. Rare earths: Jewels for functional materials of the future. *New J. Chem.* **2011**, *35*, 1165–1176. [[CrossRef](#)]
55. Rinehart, J.D.; Long, J.R. Exploiting single-ion anisotropy in the design of f-element single-molecule magnets. *Chem. Sci.* **2011**, *2*, 2078–2085. [[CrossRef](#)]
56. Richardson, M.F.; Wagner, W.F.; Sands, D.E. Rare-earth tris(hexafluoroacetylacetonates) and related compounds. *J. Inorg. Nucl. Chem.* **1968**, *30*, 1275–1289. [[CrossRef](#)]
57. Sheldrick, G.L. SHELXT—Integrated space-group and crystal-structure determination. *Acta Crystallogr. Sect. A* **2015**, *71*, 3–8. [[CrossRef](#)]
58. Sheldrick, G.M. Crystal structure refinement with SHELXL. *Acta Crystallogr. Sect. C* **2015**, *71*, 3–8. [[CrossRef](#)]
59. Te Velde, G.; Bickelhaupt, F.M.; Baerends, E.J.; van Gisbergen, S.J.A.; Fonseca Guerra, C.; Snijders, J.G.; Ziegler, T. Chemistry with ADF. *J. Comput. Chem.* **2001**, *22*, 931–967. [[CrossRef](#)]
60. Fonseca Guerra, C.; Snijders, J.G.; te Velde, G.; Baerends, E.J. Towards an order-N DFT method. *Theor. Chem. Acc.* **1998**, *99*, 391–403. [[CrossRef](#)]
61. Baerends, E.J.; Ziegler, T.; Atkins, A.J.; Autschbach, J.; Bashford, D.; Baseggio, O.; Bérces, A.; Bickelhaupt, F.M.; Bo, C.; Boerritger, P.M.; et al. *ADF2017, SCM, Theoretical Chemistry*; Vrije Universiteit: Amsterdam, The Netherlands, 2017.
62. Van Lenthe, E.; Baerends, E.J.; Snijders, J.G. Relativistic Regular two-component Hamiltonians. *J. Chem. Phys.* **1993**, *99*, 4597–4610. [[CrossRef](#)]
63. Perdew, J.P.; Burke, K.; Ernzerhof, M. Generalized Gradient Approximation Made Simple. *Phys. Rev. Lett.* **1996**, *77*, 3865–3868. [[CrossRef](#)]
64. Van Lenthe, E.; Baerends, E.J. Optimized Slater-type basis sets for the elements 1–118. *J. Comput. Chem.* **2003**, *24*, 1142–1156. [[CrossRef](#)] [[PubMed](#)]

